Boreal Summer Intraseasonal Phases Identified by Nonlinear Multivariate Empirical Orthogonal Function–Based Self-Organizing Map (ESOM) Analysis

JUNG-EUN CHU

Division of Earth Environmental System, College of Natural Science, and Research Center for Climate Sciences, Pusan National University, Busan, South Korea

BIN WANG

International Pacific Research Center, and Department of Meteorology, University of Hawai'i at Mānoa, Honolulu, Hawaii, and Earth System Modeling Center, Nanjing University of Information Science and Technology, Nanjing, China

JUNE-YI LEE

Research Center for Climate Sciences, Pusan National University, Busan, South Korea

KYUNG-JA HA

Division of Earth Environmental System, College of Natural Science, Research Center for Climate Sciences, and Department of Atmospheric Sciences, Pusan National University, Busan, South Korea

ABSTRACT

This study develops an empirical orthogonal function (EOF)-based self-organizing map (SOM) (ESOM) analysis to identify the nonlinear characteristics of the boreal summer intraseasonal oscillation (BSISO), which involves interactions between the summer mean circulation and the convectively coupled equatorial waves, which make BSISO evolution more complex than the Madden–Julian oscillation. The method utilizes the first five principal components of the outgoing longwave radiation (OLR) and the zonal wind at 850 hPa (U850) and has the advantages of filtering out uncertainties from noise and being free from mathematical restrictions, such as orthogonality and linearity.

The ESOM analysis enables the detection of BSISO over the Asian summer monsoon region with eight phases. The four most distinguishable phases represent 1) a pair of stationary patterns with a dipole between the eastern Indian Ocean and the Philippine Sea (phases 1 and 5) and 2) a pair of propagating patterns with a northwest–southeast-tilted rain belt structure (phases 3 and 7). Phases 1 and 5 show an alternating seesaw oscillation throughout the summer with a 30–60-day period, whereas phases 3 and 7 peak in mid-June and early June denoting the monsoon rainy season and premonsoon period of Asian summer monsoon. ESOM captures that phases 1 and 5 happen more frequently and last longer than phases 3 and 7, whereas multivariate EOF analysis fails to describe this nonlinear occurrence. Phases 3 and phase 7 display distinct asymmetries in convective activity over the eastern Indian Ocean related to the relatively slow-growing and fast-decaying convective activity. The relationship with large-scale SST forcing is also discussed.

1. Introduction

The boreal summer intraseasonal oscillation (BSISO) is a dominant mode of intraseasonal variability in the tropics during the boreal summer [May to October (MJJASO)] (Wang and Xie 1997; Kemball-Cook and Wang 2001; Lee et al. 2013). The BSISO is known to affect climate variability, including the summer monsoon onset (Wang and Xie 1997; Kang et al. 1999), the active/break phases of the summer monsoon (Annamalai and Slingo 2001; Ding and Wang 2009), extreme wet and dry events (Hsu et al. 2016, 2017, manuscript submitted to *J. Climate*), and climate predictability for precipitation (Wang et al. 2009; Lee et al. 2010, 2013). While the boreal winter intraseasonal

Corresponding author e-mail: Prof. Kyung-Ja Ha, kjha@pusan.ac.kr

oscillation known as the Madden–Julian oscillation (MJO) is characterized by an eastward propagation of deep convection with an approximate 30–60-day period (Madden and Julian 1972; Lau and Chan 1986), the BSISO exhibits more complex features than MJO because it involves interactions between Asian summer monsoon (ASM) circulation and convectively coupled equatorial waves. The BSISO tends to have a northward/northeastward propagation over the Indian summer monsoon (ISM) region (Yasunari 1979, 1980; Lau and Chan 1986; Wang et al. 2005) and a northward/northwestward propagation over the western North Pacific–East Asian region (Wang et al. 2001; Kajikawa and Yasunari 2005; Yun et al. 2009, 2010). This northward propagation makes the BSISO evolution more complex as it interacts with the ISM and the East Asian summer monsoon (EASM).

A number of statistical studies have attempted to explain the characteristics of the BSISO in terms of their spatial patterns and propagation. By using empirical orthogonal function (EOF) analysis, Lau and Chan (1986) found that the dominant EOF modes of outgoing longwave radiation (OLR) over the Indian Ocean–western Pacific region during the northern summer showed a dipole pattern with the convection centered over the Indian Ocean and the western Pacific–South China Sea. In addition, they showed that the first two leading modes describe different phases of the same large-scale phenomenon (i.e., eastward and northward propagation) and the EOF1 time series leads that of the EOF2 by about 10 to 15 days. Wang et al. (2005) applied a composite method using 28 selected convective events with reference to the eastern equatorial Indian Ocean and showed the propagating characteristics of BSISO using consecutive phases of the events with a 4-day interval (the mean interval of two adjacent phases). However, the periods of the individual cycles were notably irregular. Therefore, if the individual periods of a cycle in the real world do not have a regular interval, previous studies (Lau and Chan 1986; Wang et al. 2005) could not fully describe the irregular nature of the convective phases, such as the interaction with the ASM. In contrast to the previous studies, Lee et al. (2013) suggested two real-time BSISO indices that are capable of describing a large fraction of the total intraseasonal variability in the ASM region based on multivariate EOF (MV-EOF) analysis of the daily anomalies of the OLR and the zonal wind at 850 hPa (U850). However, the results of the EOF-based principal component analysis (PCA) are constrained by the orthogonality and sometimes miss information regarding the asymmetry of opposite phases and the nonlinear spatiotemporal features (Oettli et al. 2014).

To overcome the shortcomings of the linear analysis, a self-organizing map (SOM) based on an unsupervised neural network (Kohonen 1982, 1990) appears to be an effective method for feature extraction and classification (Chattopadhyay et al. 2008, 2013; Joseph et al. 2011; Chu et al. 2012; Borah et al. 2013; Johnson 2013; Sahai et al. 2014). Liu et al. (2006) evaluated the performance of the SOM in extracting linear progressive sine waves by using artificial data and demonstrated that the SOM extracts the essential patterns from noisy data in comparison to the EOF. This is because the SOM-derived patterns are local in nature, which means the SOM patterns are not dependent on a covariance matrix as required in the EOF or extended EOF (EEOF) analyses (Kohonen 1997; Sahai et al. 2014). Therefore, the application of the SOM technique to extract monsoon intraseasonal characteristics would be free from various mathematical restrictions, such as orthogonality and linearity in the EOF analysis (Chu et al. 2012).

The main purpose of this study is to apply an EOF-based nonlinear SOM analysis, named by ESOM, to detect the BSISO phases without restrictions of linearity and orthogonality. The method first performs EOF analysis of the OLR and U850 over the ASM region and then applies the derived principal component (PC) time series to the SOM analysis. The EOF analysis acts as a filter that removes the uncertainties from transient eddies and noisy patterns. Therefore, the ESOM can readily obtain physically meaningful patterns while conserving major low-frequency variability. In addition, applying the PC time series instead of the EOF patterns reduces the computational time while conserving the dominant modes. Recently, Sahai et al. (2014) developed a SOM-based PCA analysis to obtain the linearly decorrelated PCs of the EOFs of the monsoon intraseasonal oscillation. Our ESOM analysis is different from the method applied in Sahai et al. (2014) because their method uses the SOM-based local PCA analysis and is statistically similar to an EEOF analysis. Our result will be qualitatively compared with a linear EOF analysis in addition to the MV-EOF analysis conducted by Lee et al. (2013).

2. Data and method

a. Data

The data used for the ESOM analysis included the daily Advanced Very High Resolution Radiometer (AVHRR) OLR data with 2.5° horizontal resolution from the National Oceanic and Atmospheric Administration (NOAA) polar-orbiting satellites (Liebmann and Smith 1996) and the U850 data from the NCEP–Department of Energy (DOE) AMIP-II reanalysis

(Kanamitsu et al. 2002) with $2.5° \times 2.5°$ horizontal resolution.

Data from May to October were used in the diagnostics of the BSISO. For a given field, its daily anomalous time series was generated by the same method used by Lee et al. (2013), which removes its annual cycle (the mean and first three harmonics of the climatological annual variation) as well as the interannual variability by subtracting the running mean of the previous 120 days as in Wheeler and Hendon (2004). After that, the two anomaly fields were normalized by their area-averaged temporal standard deviation over the ASM region (10°S–40°N, 40°–160°E). The normalization factors are $31.79 \, \text{W m}^{-2}$ for OLR and $3.81 \, \text{m s}^{-1}$ for U850. No intraseasonal bandpass filtering was applied to the data.

b. ESOM analysis

This study develops an ESOM using a synthetic PC time series of two different variables, OLR and U850, to obtain the nonlinear and asymmetric behavior of the BSISO. The SOM is an unsupervised artificial neural network and a useful tool in reducing a high-dimensional dataset into a low-dimensional version to summarize the key aspects of the larger dataset (Kohonen 1982, 1990, 1997; Oettli et al. 2014). The method has been successfully applied to climate research, including in the MJO (Chattopadhyay et al. 2013, Oettli et al. 2014), the EASM (Chu et al. 2012; Oh and Ha 2015), the ISM (Chattopadhyay et al. 2008; Borah et al. 2013; Joseph et al. 2011; Sahai et al. 2014), and the El Niño–Southern Oscillation (ENSO) (Johnson 2013).

The principal steps in an ESOM analysis are as follows: given any data matrix $\mathbf{D}(\mathbf{s}, \mathbf{t})$, where $\mathbf{s}$ represents a spatial dimension (e.g., latitude and longitude) and $\mathbf{t}$ represents the time coordinates, the EOF can be described as follows:

$$\mathbf{D}(\mathbf{s}, \mathbf{t}) = \mathbf{D}'(\mathbf{s}, \mathbf{t}) + \text{residual}$$

$$\mathbf{D}'(\mathbf{s}, \mathbf{t}) = \sum_{i=1}^{N} \text{EOF}_i(\mathbf{s}) \times \text{PC}_i(\mathbf{t}),$$

where N is the number of major modes and $\mathbf{D}'$ represents the filtered data. The degree of filtering depends on the value of N. In this study, we use the OLR and U850 daily anomalies over the ASM region (10°S–40°N, 40°–160°E) from 1 May to 31 October for a 30-yr period (1981–2010) as the input $\mathbf{D}$. The number of PCs (N) selected is 5, based on the consideration that N is large enough to capture the major observed daily fields and small enough to conveniently extract the ISO phases. A sensitivity test for the selection of the optimal value of N will be discussed in section 2c.

After conducting the EOF analysis, we prepare the synthetic PC time series of the daily OLR and U850 as an input for the SOM analysis as schematically shown below:

$$\mathbf{X}(\mathbf{s}, \mathbf{t}) = \begin{bmatrix} \text{PC}_{\mathbf{s}=1,\mathbf{t}=1}, \text{PC}_{\mathbf{s}=2,t=1}, & \cdots & \text{PC}_{\mathbf{s}=2N,\mathbf{t}=1} \\ \vdots & \ddots & \vdots \\ \text{PC}_{\mathbf{s}=1,\mathbf{t}=M}, \text{PC}_{\mathbf{s}=2,\mathbf{t}=M} & \cdots & \text{PC}_{\mathbf{s}=2N,\mathbf{t}=M} \end{bmatrix},$$

where $\mathbf{X}$ is an input of the SOM analysis, $\mathbf{s}$ is the input vector where the size of the input vector corresponds to the total number of PCs $2N$ (here it is 10 including 5 PCs from the OLR and 5 PCs from the U850), $\mathbf{t}$ is the input sample that corresponds to the time where the size of time corresponds to total number of days M (184 days $\times$ 30 yr = 5520 days). The SOM trains the large number of input vectors $\mathbf{X}(\mathbf{s}, \mathbf{t})$ to be projected to a reduced number of output arrays (mostly two-dimensional space) and classifies the input samples into the two-dimensional space. The output array represented in two-dimensional space is called a map and the individual vector that has the same size as the input vector (i.e., $2N$) is called a reference vector or a weighing vector. After testing different sizes, we selected a 3×3 map following Chattopadhyay et al. (2008, 2013) and Chu et al. (2012), who described that a 3×3 map is optimal for describing intraseasonal variability and its life cycle. At the first stage, the reference vectors are randomly initialized. The final reference vectors are obtained through an iterative training process. During the iterative process, a node with the smallest Euclidean distance (EUD) with respect to the input data is identified:

$$\text{EUD} = |\mathbf{X} - \mathbf{W}_j| = \sqrt{\sum_{i=1}^{2N} (\mathbf{X}_i - \mathbf{W}_{ij})^2},$$

where $\mathbf{X}$ is the input vector, $\mathbf{W}_j$ is the reference vector, and i and j correspond to the index for the position on the vector and map, respectively. The reference vector with the smallest Euclidean distance updates the reference vector and its associated weights together with those of the neighbor nodes within the neighborhood radii. Since each reference vector has to be adjusted relative to its neighbor, inclusion of the neighborhood makes the SOM classification nonlinear compared to other clustering analyses. The updated equations for the reference vector are described as follows:

$$\mathbf{W}_j(n + 1) = \begin{cases} \mathbf{W}_j(n) + c(n)[\mathbf{X}(n) - \mathbf{W}_j(n)], & j \in \mathbf{R}_j(n) \\ \mathbf{W}_j(n), & \text{otherwise} \end{cases}.$$

In this reference vector for the nth training cycle, $\mathbf{R}_j(n)$ is the predefined neighborhood around the reference

vector j, and $c(n)$ is the neighborhood kernel, which defines the neighborhood. The neighborhood kernel may be a monotonic decreasing function of n $(0 < c(n) < 1)$, known as a bubble, or it may be of a Gaussian type as follows:

$$\alpha(n) \exp\left[\frac{-\|r_j - r_i\|^2}{2\sigma^2(n)}\right],$$

where $\alpha(n)$ and $\sigma(n)$ are constants that monotonically decrease with n. In this equation, $\alpha(n)$ is the learning rate, which determines the velocity of the learning process, while $\sigma(n)$ is the amplitude, which determines the width of the neighborhood kernel. In addition, r_j and r_i are the coordinates of the reference vectors j and i, respectively, in which the neighborhood kernel is defined. Throughout training, the learning rate and the size of the update neighborhood (the update radius) decrease, leading to progressively refined initial generalized patterns. Finally, the SOM consists of a number of patterns that are characteristic of the data, with similar patterns nearby and dissimilar patterns farther apart. After the training process, the final output arrays (i.e., map) represented in two-dimensional space is completed. The mapping process distributes each input vector to a corresponding reference vector based on its similarity (i.e., the least Euclidean distance). In this way, the reference vectors in a self-organizing map compete to most effectively represent input samples. The schematic diagram of the SOM algorithm is described in Chu et al. (2012). A detailed mathematical description of the SOM algorithm is found in Kohonen (1982, 1990).

At the end of clustering, we obtain a 3×3 map, and the index of location for individual input vector best-matched to reference vector. In our case, the input data consist of 5520 vectors, made up of daily OLR and U850 PCs from 1 May to 31 October for the period 1981–2010. To enhance the visualization, the composite of the classified dates provides a spatial structure for each phase; that is, if the summer monsoon ISO is a convectively coupled oscillation, each pattern should be strongly related to a particular phase of the precipitation oscillation. Therefore, the ESOM analysis has advantages in filtering out uncertainties from high-frequency noise and being free from mathematical restrictions, such as orthogonality and linearity as in an EOF-like analysis. In addition, the use of the synthetic PC time series of OLR and U850 enables a multivariate approach that illuminates the interrelatedness between and within sets of variables while reducing computational time. Through the sensitivity test, we found that the computational time for ESOM analysis using synthetic PC time series of OLR

and U850 is 10 times faster than the analysis using spatial pattern of OLR or U850.

c. Sensitivity tests

To determine the optimal number of PCs, we compared the sensitivity of the number of PCs between ESOM and MV-EOF analysis in Fig. 1. The idea of the sensitivity test is to compare results derived from the ESOM analysis and the MV-EOF analysis in terms of consistencies in the horizontal patterns and percent variances. For this purpose, we conducted nine different ESOM experiments by altering the number of PCs (N) used as input vectors from 2 to 10. If we assume that the horizontal pattern of the ISO modes and their percent variance are no longer sensitive to N after a critical value, we can compare the horizontal patterns and percent variance of the four major modes when $N = 10$ with the other experiments (i.e., $N = 2$ to $N = 9$). For the sensitivity test of the MV-EOF analysis, the four leading EOF patterns are compared with original OLR anomaly fields reconstructed using 2 to 10 PCs.

The results show that there are strong consistencies in the ESOM patterns and the percent variances of the four major modes even if we decrease the number of PCs to $N = 5$. However, the consistencies abruptly decrease when $N < 5$. In contrast, the pattern similarities of the MV-EOF modes are stable up to $N = 6$, but the percent variances are either exponentially or abruptly changed as the number of reconstructed PCs decreases. Therefore, we conclude that five PCs are needed for consistencies in the ESOM patterns and the percent variances. More than five PCs are likely unnecessary.

Another issue is the selection of variables for the BSISO used in the ESOM analysis. In this study, we used OLR and U850 as representative variables of BSISO as in Lee et al. (2013) for the MV-EOF analysis. The leading EOF modes of the northward wind at 850 hPa (V850) or the zonal wind at 200 hPa (U200) do not have strong signals over the tropical region but are strong in the midlatitude EASM area. Inclusion of V850 and OLR provides the BSISO components weighted for the EASM (figure not shown). Therefore, we use OLR and U850 as major variables in detecting the BSISO modes using the ESOM analysis.

3. Comparison of BSISO features extracted by ESOM and EOF analysis

a. BSISO described by EOF analysis

Figures 2a and 2b show spatial patterns of the first five leading EOF modes for the daily OLR and U850 anomalies over the ASM region (10°S–40°N, 40°–160°E), respectively. The horizontal structure of the
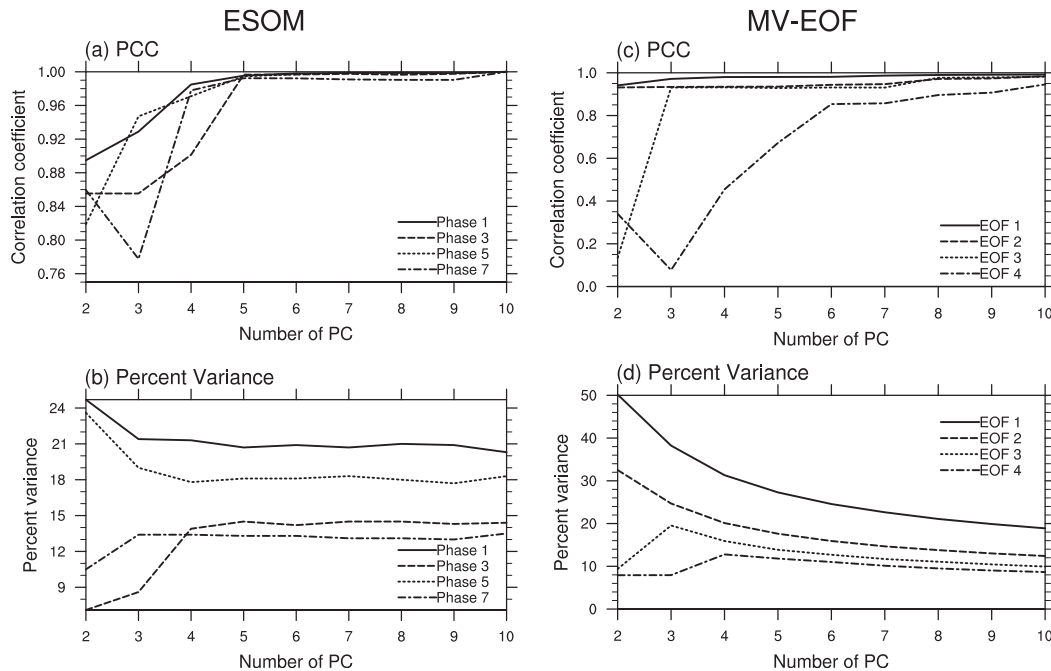
FIG. 1. Sensitivity tests for (a),(b) ESOM and (c),(d) MV-EOF analysis in terms of maximum (top) pattern correlation coefficients (PCC) and (bottom) percent variance of four major modes. The maximum PCCs for ESOM are calculated by comparing spatial structure of 10-PC experiments with others from 2- to 10-PC experiments. The maximum PCC for the MV-EOF four major modes using reconstructed data with 2- to 10-PC are compared with the spatial structure of the 10-PC MV-EOF experiment.

EOF1 of the OLR shows an east–west-oriented dipole with two centers over the eastern Indian Ocean and the Philippine Sea with opposite polarities. Their percentage variance has a fairly low value of 5.5% because the EOF analysis is applied to daily unfiltered data. In the EOF2 of the OLR, the centers of the east–west dipole are slightly displaced northward, displaying a narrow band structure tilted from the Indian subcontinent to the southeastern Philippine Sea. In contrast, the EOF3 and EOF4 of the OLR show a southwest–northeast-tilted horizontal structures stretching from the equatorial Indian Ocean to the South China Sea. The EOF5 shows a north–south contrast over the Indian Ocean and a northwest–southeast contrast over the western Pacific/South China Sea region. The first five OLR EOF modes together explain 19% of the total daily variance. The U850 components of the first two EOF modes support the convectively coupled characteristics with westerly anomalies occurring to the north of the positive OLR anomalies and vice versa for the easterlies (Fig. 2b). The U850 fields support the coupling between the circulation and convection; however, the southwest–northeast tilting of the winds in EOF3 and EOF4 is more prominent in the western North Pacific than in the Indian Ocean. The EOF5 of U850 does not appear to be a physically meaningful pattern and maybe a

computationally generated higher-order mode as a function of the domain size.

The first and second (the third and fourth) EOF modes of OLR and U850 resemble the two components of BSISO1 (BSISO2) identified by Lee et al. (2013). In that study, they treated the first two modes as a pair and described them as a canonical northward-propagating BSISO component. The lag correlation coefficient between PC1 and PC2 reveals that PC1 and PC2 have greatest coherence in the 30- to 60-day range with a 90° phase difference indicating that PC1 leads PC2 by a quarter of cycle. It supports the arguments in Lee et al. (2013) that the first two modes are different phases of the same large-scale phenomenon, which reflects northward propagation. They also noted the EOF3 and EOF4 describe the northwestward propagation of convection and interaction with the EASM and named the EOF3 and EOF4 modes as the ASM premonsoon and onset components, respectively. Although the EOF analysis as shown in Fig. 2 is capable of explaining large-scale dominant patterns such as northward and northwestward propagation to some degree, it is hard to demonstrate how they interact with the ASM system.

b. BSISO described by ESOM analysis

In this section, we present the major BSISO patterns obtained by the ESOM analysis. ESOM provides
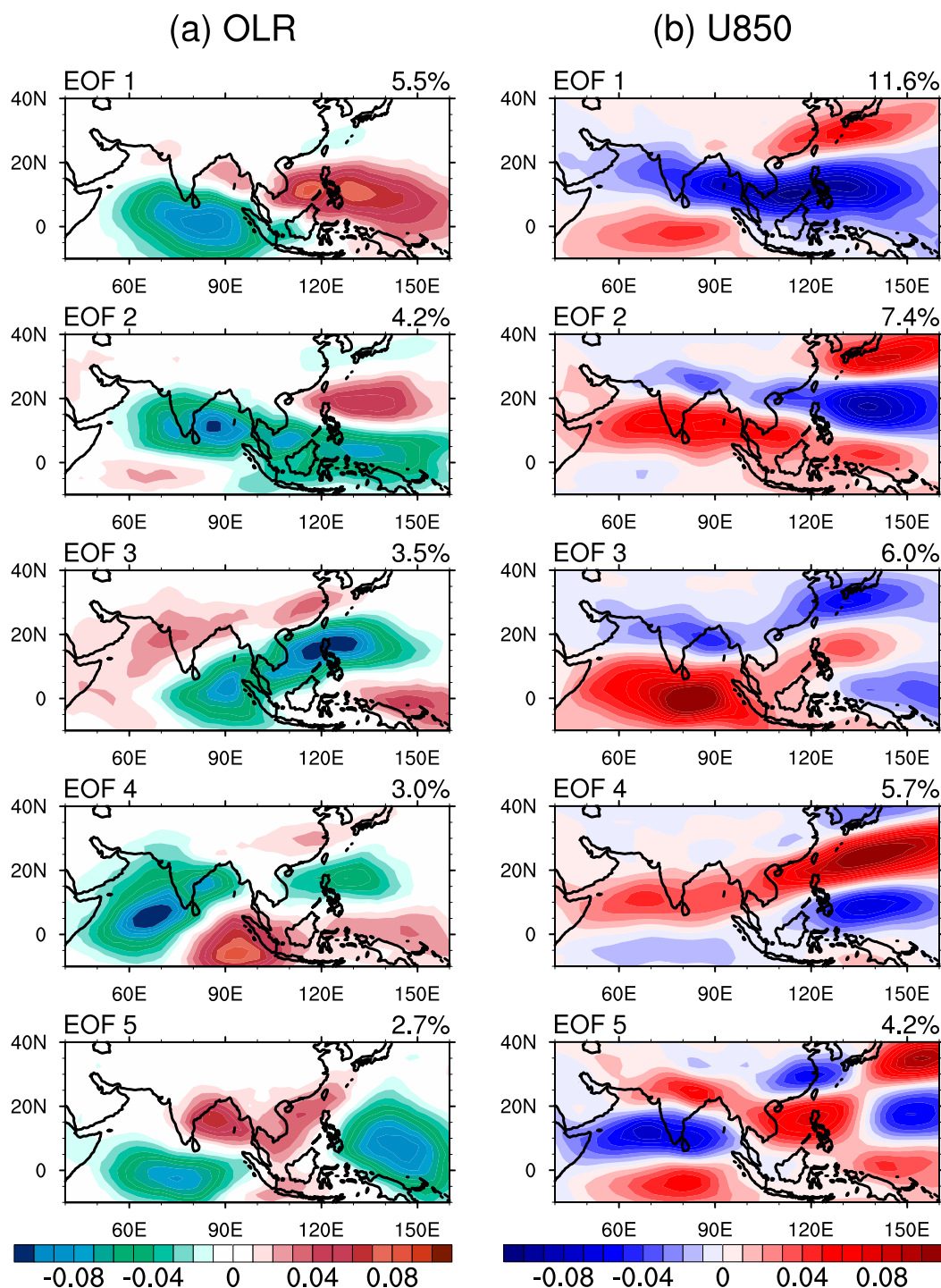
(a) OLR   (b) U850

FIG. 2. Spatial structure of the five leading EOF modes of daily (a) OLR and (b) U850 anomalies over the ASM region (10°S–40°N, 40°–160°E). The EOF modes were obtained during MJJASO for the 30 years of 1981–2010.

information about most frequently observed spatial patterns of BSISO. After training a large number of input vectors, we obtain the nine patterns distributed in a two-dimensional 3 × 3 lattice. The trained vectors in

each panel are called the reference vectors, which have the same size with input vectors but with the reduced number of patterns. In other words, the reference vectors in the 3 × 3 lattice are nine representative patterns

of the total number of samples (i.e., 184 days × 30 yr = 5520 days). Each reference vector corresponds to the combined PCs, five from the OLR and the other five from the U850. As shown in Fig. 3, the 3 × 3 reference vectors have unique combinations of PCs, which are predominantly separated by first two PCs of OLR and U850. For instance, (0,0) and (2,2) are characterized by the large magnitude of PC1 of both OLR and U850, while (2,0) and (0,2) have relatively comparable (larger) magnitudes of PC2 of OLR (U850) than those of PC1. In addition, the reference vectors located at the diagonally opposite side tend to have opposite signs, though it is not exactly a mirror image.

The composite patterns of OLR and winds at 850 hPa identified by ESOM analysis are displayed in Fig. 4. The patterns are obtained by compositing OLR and winds at 850-hPa anomalies corresponding to the days classified at each mode (see section 2b for more details on methodology). As will be mentioned later, each pattern represents the individual BSISO phase, and they together describe a phase evolution of BSISO following a clockwise direction. For this reason, we will call each panel a ''phase'' for more readable understanding of physical phenomenon. We also named each pattern phase 1, phase 2, through phase 8 following a clockwise direction starting from the top left-hand corner. The percentages to the top right of each panel refer to the frequency of occurrence (the number of clustered days divided by the number of total days for the 30-yr period). Therefore, summing all of the percentages gives 100%.

The four phases at the corners tend to have larger percentages than those in the middle panels. This is because the SOM tends to locate similar patterns nearby and dissimilar patterns farther away according to the neighborhood function. As a result, dominant phases tend to be located at the corner with the most different phases located at the opposite corner. The dominant phases located in the corner (i.e., phases 1, 3, 5, and 7) have a total variance greater than 13%, and they are similar to the first and second modes in the EOF analysis with opposite polarities. Phases 1 and 5 explain 20.9% and 18.2% of the total, respectively. The horizontal patterns of phases 1 and 5 show a pair of stationary patterns with a dipole between the eastern Indian Ocean and the Philippine Sea. Although the percent explained by phase 1 is 2.7 percentage points higher than that of phase 5, their spatial patterns and percentages show a symmetric system of the tropical convection during boreal summer. Phases 3 and 7 have a quadrupole structure characterized by northwest to southeast tilted structure as identified in the EOF2.

These two pairs of ESOM patterns are similar to the first two leading MV-EOF modes, but they also show important differences. Although the northwest-to-southeast slope of the anomalous convection in phases 3 and 7 seems to have an opposite pattern, considerable differences are found over the equatorial eastern Indian Ocean. In phase 3, strong monsoonal flows are found over both the ISM and EASM regions. Intense low-level southwesterly winds in the Arabian Sea bring heavy rainfall to India, related to the annual occurrence of the ASM rainy season. However, phase 7 has a weak signal in convection and circulation over the Indian Ocean while frontal convection extends from the South China Sea to southeastern Japan. The zonally elongated narrow convection zone over the northeast Asian region in phase 7 shows a similar structure to the premonsoon states of the ISM and EASM. The physical meaning of the asymmetries in the eastern Indian Ocean will be discussed in section 4.

The middle panels, including phases 2, 4, 6, and 8, have lower percentages than those at the corner, covering only 7%–8% of the total variance. Their patterns are intermediate between two adjacent phases. While phases 2 and 6 have strong signals over the western North Pacific region, phases 4 and 8 have extended convection over the equatorial central Indian Ocean. The pattern in the center does not have a meaningful spatial structure and the percent variance is the smallest (only 2.4%). Therefore, it will be regarded as random noise.

4. New features of BSISO revealed by ESOM analysis

a. Preferred seasonal occurrence and phase-locking to annual cycle

The ESOM analysis provides dates clustered to the most similar pattern in addition to the 3 × 3 patterns; it is possible to examine the preferred seasonal occurrence and phase locking to annual cycle. Figure 5 shows the occurrence of each phase by accumulating the number of clustered days from May to October. Phases 1 and 5 have a regular oscillation with a 30–60-day period. It is interesting to note that phases 1 and 5 show alternating oscillations throughout the whole summer with an approximately 30-day period. The seasonally phase-locked temporal variations of phases 1 and 5 support the existence of the climatological intraseasonal oscillation suggested by Wang and Xu (1997). It is interesting to note that phase 5, which has strong (weak) convective activity center over the western North Pacific (Indian Ocean) shows constant occurrence time series during late boreal summer (August–October) because the
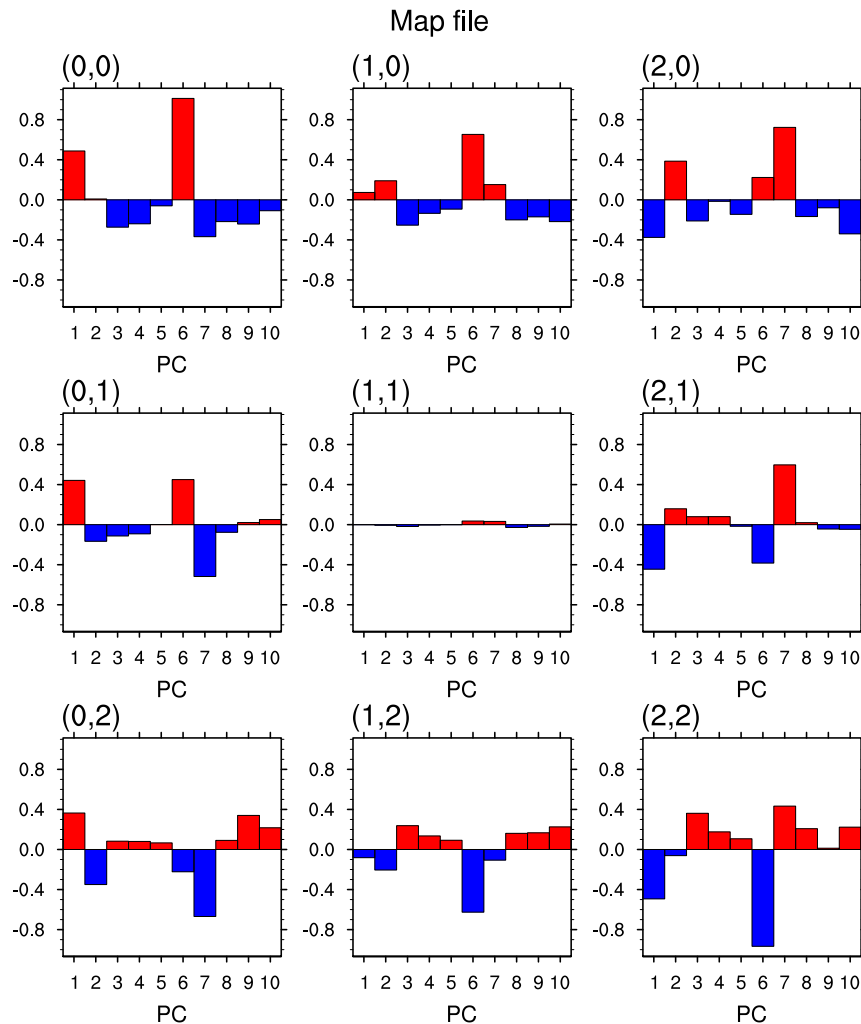
Map file

FIG. 3. The 3 × 3 reference vectors trained by the ESOM. The size of reference vector is 10 and is composed of five OLR and five U850 PCs.

western North Pacific seasonal mean monsoon trough plays an essential role in sustaining a strong stationary ISO (Liu and Wang 2014).

On the contrary to stationary phase 1 and phase 5, the preferred seasonal peaks are apparent in phase 3 and phase 7. A large number of phase-3 events are concentrated from mid-June to mid-July, and the strongest peak occurs in mid-June. Those peaks correspond to the period of active and break phases of the ISM and EASM, which is accompanied by small and large water fluxes across the Arabian Sea and subtropical western North Pacific. Phase 7 has one prominent peak in early June, and this period corresponds to the preonset period of ISM and EASM. Previously, Lee et al. (2013) defined the third and fourth modes of the MV-EOF results as the ASM premonsoon and onset component and considered the northward-propagating BSISO and ASM

onset separately. Lee et al. (2013) showed that 18 out of 28 cases of the Indian monsoon onset (i.e., 64%) tend to occur in phases 2–4 of BSISO2. Our results show that the phase locking of the ASM is also embedded in the occurrence of phases 3 and 7. This argument is further supported by Fig. 6.

Figure 6 displays the composite spatial pattern of the OLR and U850 during the premonsoon and rainy season of ASM, which correspond to the peak periods of phase 7 and phase 3 in Fig. 5, respectively. The peak period for phase 7 is from 25 May to 5 June, while that for phase 3 is from 10 to 20 June. Previously, it was suggested that the whole procedure of the outbreak of the Asian monsoon onset is composed of three consecutive stages: first over the Bay of Bengal in early May, then over South China Sea in mid-to-late May, and last over Indian continent in mid-June (Wu and Zhang, 1998; Liu et al. 2002; Liu et al.

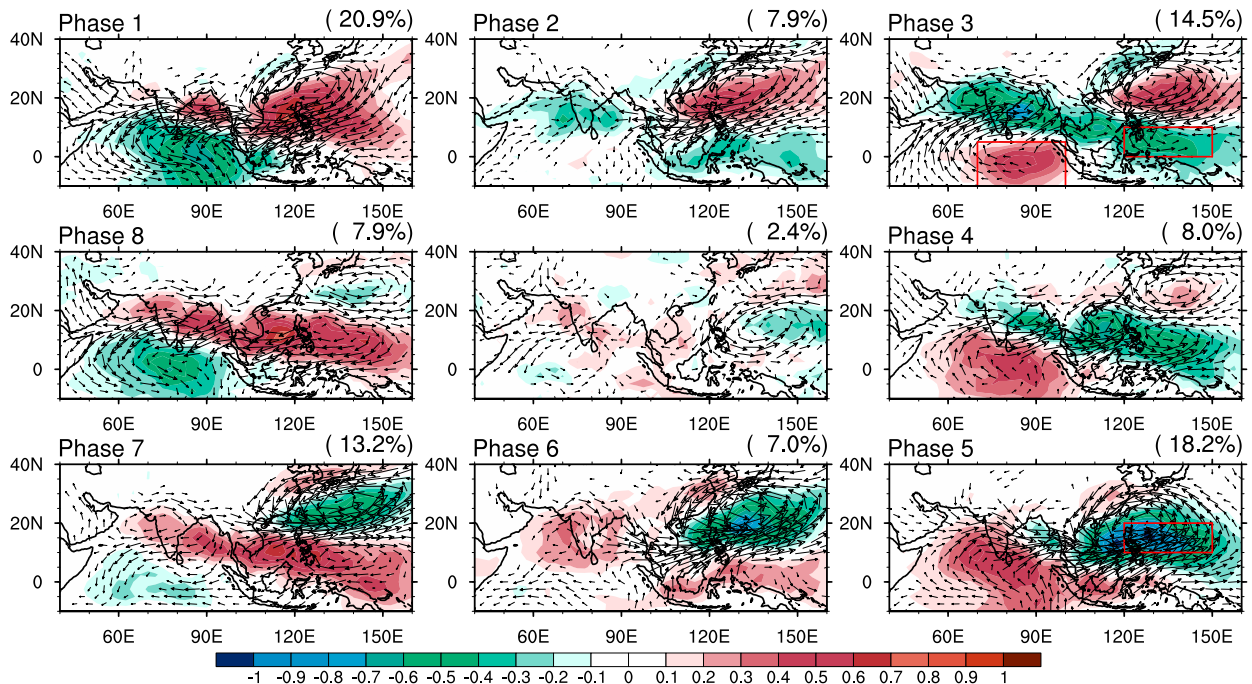## Composite E-SOM patterns (OLR & 850-hPa Wind)

FIG. 4. The nine patterns of OLR (shading) and 850-hPa wind (vector) anomalies identified by the ESOM. The patterns are obtained by compositing anomalies corresponding to the days clustered at the respective modes. Since each pattern represents the individual BSISO mode and they together describe a phase evolution of BSISO following a clockwise direction, each pattern is named phase 1, phase 2, through phase8 following a clockwise direction starting from the top left-hand corner. The percentages in the top right of each phase refer to the frequency of occurrence of the pattern for the 1981–2010 period. Red boxes in phases 3 and 5 indicate the equatorial western Indian Ocean, western Pacific Ocean, and western North Pacific Ocean selected for Fig. 9.

2015). During the period of 25 May to 5 June, there are large-scale deep convection developments over the southern Arabian Sea and the oceanic region extending from the South China Sea to south of Japan. It denotes the preonset period of ISM at Kerala and the establishment of the East Asia subtropical front after the South China Sea summer monsoon onset as identified previously (Liu et al. 2002; Ding and Chan 2005; Wang et al. 2009; Liu et al. 2015). During the period from 10 to 20 June, the enhanced convection of the ISM moves northward and reaches around 15°–20°N. The variation of the 850-hPa wind over the southern Arabian Sea and East Asia is relevant to rainfall changes as a Rossby wave response to anomalous convective heating generating southwesterly flow over the Arabian Sea and western North Pacific. This period corresponding to the monsoon rainy season after grand onset of ASM identified by Wang and Xu (1997) and Linho and Wang (2002), which is characterized by the simultaneous rainfall event of the ISM over the Ganges River valley and the mei-yu/baiu in East Asia. Therefore, phases 7 and 3 explain the climatologically phase-locked ASM premonsoon and monsoon rainy season, which is

manifested in particular phases with a pair of propagating patterns.

b. Stationary and propagating characteristics revealed by ESOM

One of the most important aspects of ESOM analysis compared with EOF and other approaches is that ESOM depicts different stationary and propagating characteristics of the phases. The phase propagation of the intraseasonal phases has been shown in several studies. Lee et al. (2013) showed the life cycle of the northward-propagating BSISO by constructing a composite in a similar fashion to what was done for MJO by Wheeler and Hendon (2004). Joseph et al. (2011) depicted the propagation characteristics of the ISM intraseasonal phases by calculating probability of the propagation of each SOM phase. The BSISO, in a broad scale, is a continuum of the northward propagation which fluctuates between positive and negative convective anomalies with a 30–60-day period. However, the northward propagation exhibits large inhomogeneity in both space and time. For instance, during the ASM premonsoon and monsoon rainy

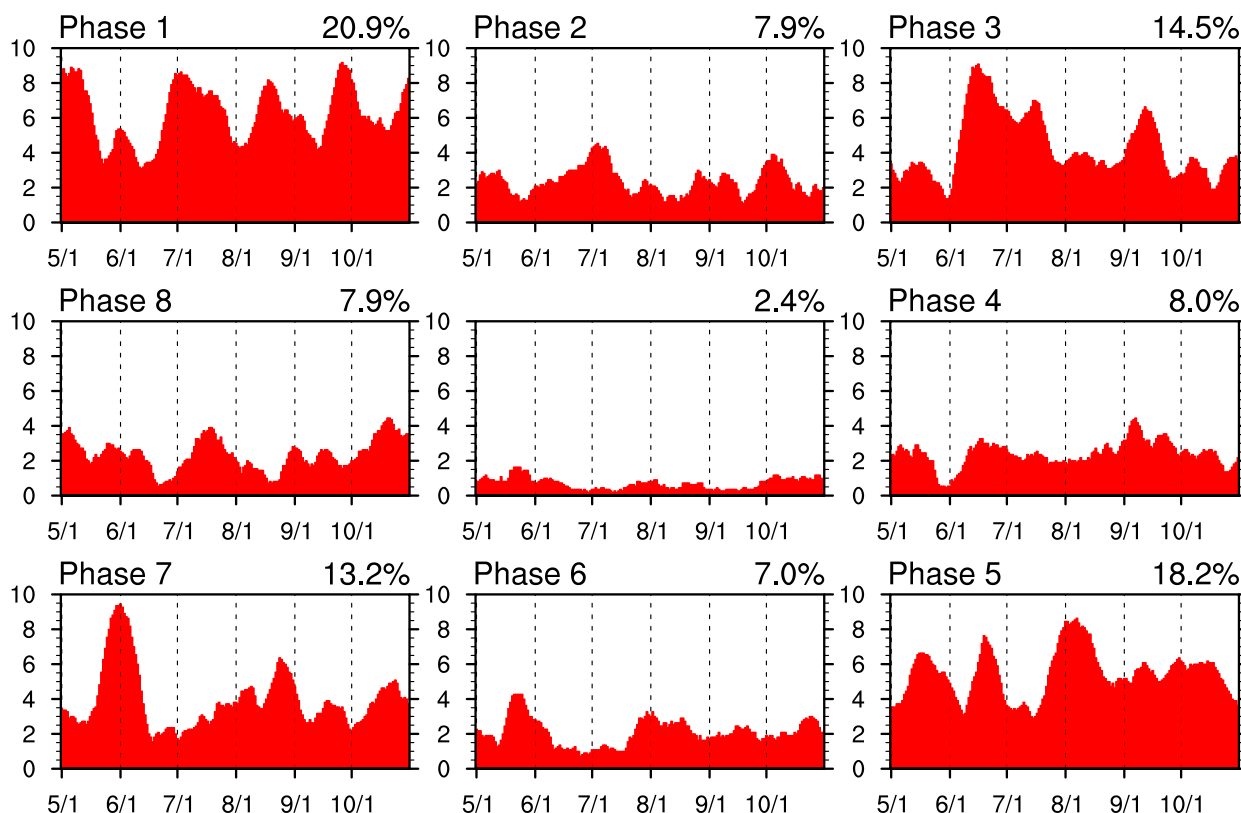## Occurrence in MJJASO (1981-2010)

FIG. 5. Occurrence time series for each of the nine ESOM phases for MJJASO based on 30 years from 1981 to 2010. An 11-day running mean was applied.

season, BSISO tends to stay in a particular pattern. These distinguished stationary characteristics of four dominant phases are an important feature of BSISO that is distinguished from MJO (Zhu and Wang 1993). Therefore, it is meaningful to examine irregular stationary and propagating features of BSISO by nonlinear ESOM analysis.

Figure 7 depicts the transition probability of propagation from one phase to the other based on the clustered days in each phase. The size of the arrow varies according to its transition probability to the direction of the each arrow. Arrows that represent less than a 5% transition probability are removed. The percentage in the top right corner indicates the probability to stay at the same phase. For example, when a particular day of summer is clustered in phase 1, 78.6% of the next day is clustered in the same phase and 9.5% of the day is moved to phase 2. It is shown that the probability to remain in one of the four phases at the corner have high percentages with more than 70%. In contrast, the probability to remain in a phase in the middle has percentages less than 50%. This indicates that the

convective activities related to the phases in the corners (i.e., phases 1, 3, 5, and 7) are more stationary than those in the middle (i.e., phases 2, 4, 6, and 8), which tend to have faster transitions. The eight phases of ESOM pattern further provide structural evolution of BSISO cycle. The arrows in eight phases in Fig. 7 tend to have maximum transition probability with clockwise direction following the path phase 1—phase 2—phase 3—...—phase 8. As will be mentioned later, the structural evolution of the eight phases explains the northward-propagating characteristics of BSISO.

Figure 8 shows the combination of the ESOM phases following a clockwise direction starting from phase 1 through phase 8 for particular longitudes over the Indian Ocean, the Maritime Continent, and the western Pacific. The direction of the phase from phase 1 through phase 8 can be simply interpreted as time evolution. It is identified that the positive and negative convection anomalies over the Indian Ocean show a strong northward propagation from 15°S to 25°N. In the Indian Ocean, the maximum convection appears between the latitudes of 5° and 10°N and gets
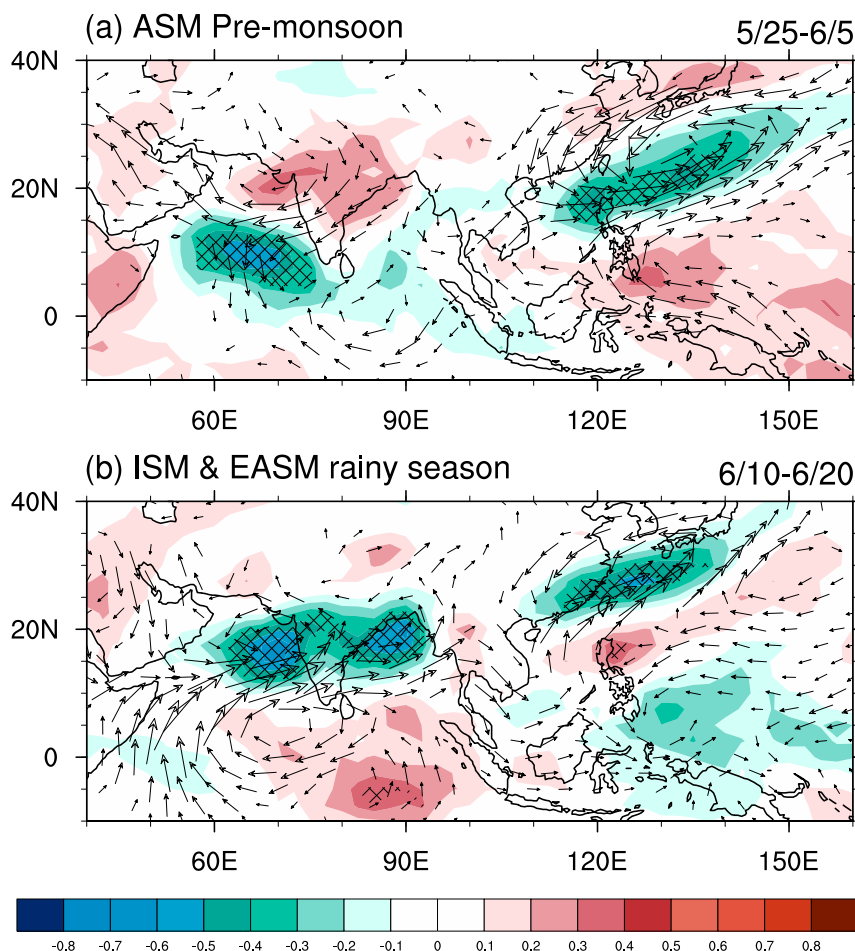
FIG. 6. Composite spatial structure of OLR (shading) and 850-hPa wind (vector) anomalies averaged during peak period of phase 7 and phase 3 in Fig. 4. The peak period for phase 7 is from 25 May to 5 June, while that for phase 3 is from 10 to 20 June. Shaded area denotes the 90% confidence interval for the standard normal distribution.

weaker as it moves northward. In addition, a slightly southward movement and a structural northward propagation are also found over the southern equatorial Indian Ocean and western Pacific region, respectively. The convection anomalies in the western Pacific also propagate northward and maintain their amplitude from the equator to 30°N. Northward propagation of convection and wind anomaly is more prominent over the western Pacific than the Indian Ocean. In contrast to the Indian Ocean and the western Pacific, convective activity over the Maritime Continent shows a sudden phase shift in phases 2 and 6. A pair of positive and negative convections is located symmetrically based on the 5°N latitudinal band from phase 2 through phase 6. From phase 6 through phase 2, however, a negative OLR is dominant near 10°N, while a weak positive convection is over the southern region.

c. Asymmetric evolution in the equatorial eastern Indian Ocean convection

In the previous section, we examined the performance of ESOM analysis in detecting the dominant characteristics of the BSISO represented in two-dimensional space, which consists of nine different phases. We also identified considerable asymmetries between phase 3 and phase 7, especially over the equatorial eastern Indian Ocean. These conspicuous asymmetric convection anomalies over the eastern Indian Ocean raise a question regarding whether this feature is an intrinsic asymmetry in Indian Ocean or not. If this is an intrinsic nonlinearity, why does this asymmetry emerge in the Indian Ocean and what does it physically tell us?

To examine the asymmetric characteristics in convective activities, we perform a composite analysis of the OLR anomaly over three convective zones, including
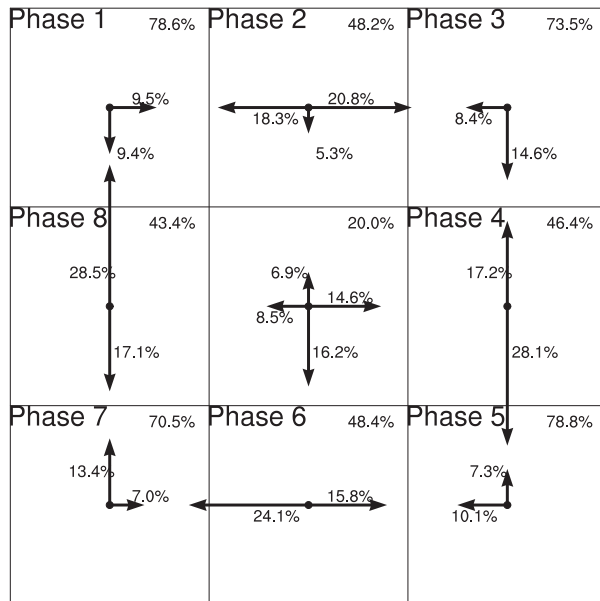
FIG. 7. Transition probability of one phase to adjacent phase based on clustered days. The size of the arrow varies according to its probability. Arrows that represent less than 5% are removed. The percentage in the top right corner indicates the probability to stay.

the equatorial eastern Indian Ocean (10°S–5°N, 70°–100°E), the western Pacific (0°–10°N, 120°–150°E), and the western North Pacific (10°–20°N, 120°–150°E). The positive OLR (dry) and negative OLR (wet) events are selected when the OLR anomalies are greater than 1 (less than −1). Figure 9 shows the composite temporal evolution of the daily OLR anomaly for dry and wet events from the day before (−25) to the day after (+25) for the maximum events over the eastern Indian Ocean, western Pacific, and western North Pacific, respectively. The wet events are multiplied by −1 for convenience. Prominent differences between the wet and dry events can be found over the eastern Indian Ocean (Fig. 9a). Over the eastern Indian Ocean, there is a slow development of wet events from approximately day −20 and a fast decay after the convection peak relative to dry events. In contrast, the dry events grow quickly and slowly decay relative to the wet events. The wet events over the eastern Indian Ocean likely recharge the convective energy slowly and discharge the potential energy in a short time and turn over to dry events. On the contrary, there are weak phase differences between the wet and dry events over the western Pacific and the western North Pacific region. It should be also noted that convective events over the eastern Indian Ocean show an oscillating characteristic, which turns the signal from negative (positive) to positive (negative) with time. This characteristic of convective activity over the Indian Ocean shows about a 30-day
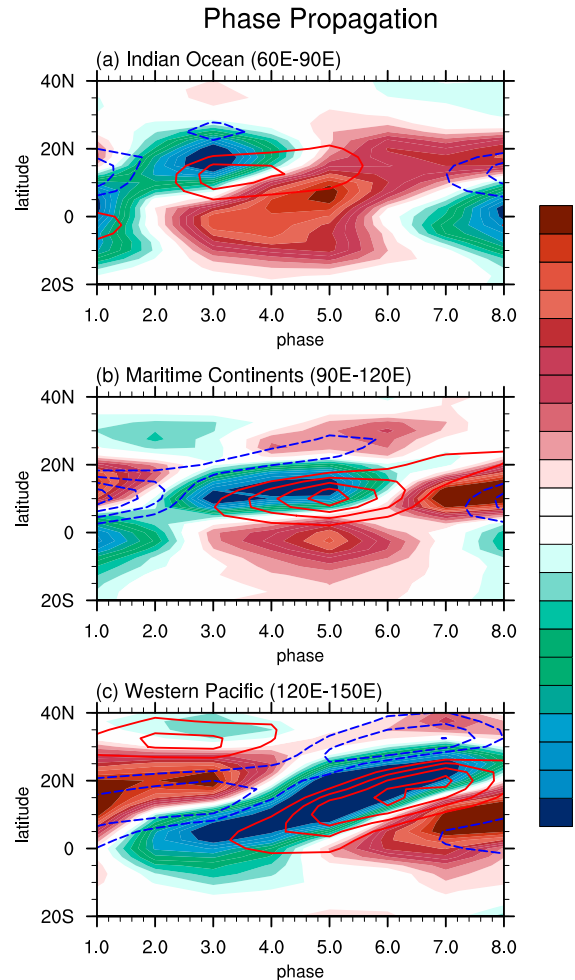

FIG. 8. Phase–latitude diagram over the (a) Indian Ocean (60°–90°E), (b) Maritime Continent (90°–120°E), and (c) western Pacific (120°–150°E). Shading represents the OLR anomalies, while the contour indicates the U850 anomalies. The phase number corresponds to mode number in Fig. 4.

period standing oscillation of tropical convection, possessing a nonlinear feature between the dry and wet events. In addition, the characteristics of the eastern Indian Ocean convective activities are not dependent on El Niño and La Niña events (figure not shown). Therefore, we argue that the asymmetry found by the ESOM analysis in the equatorial eastern Indian Ocean is an intrinsic property of the convective activities with relatively slow growth and fast decay.

d. Interannual relationship between four major phases and ENSO

On the interannual time scale, it has been reported that large-scale SST forcing such as El Niño event play a significant role in ISO activities over the Indian Ocean and western Pacific. Generally, the largest amplitude of

(a) Eastern Indian Ocean

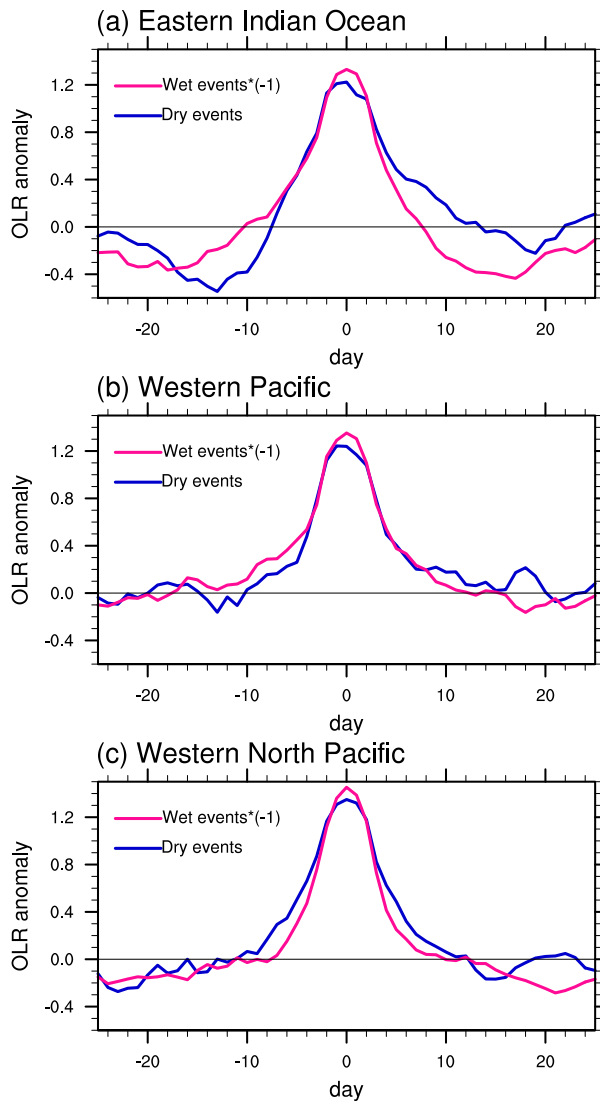## (b) Western Pacific

(c) Western North Pacific

FIG. 9. Composite temporal evolution of the daily OLR anomaly for wet events (red) and dry events (blue) from the day before (−25) to the day after (+25) the maximum events over the (a) eastern Indian Ocean (10°S–5°N, 70°–100°E), (b) western Pacific (0°–10°N, 120°–150°E), and (c) western North Pacific (10°–20°N, 120°–150°E). The wet events are multiplied by −1 for convenience. The wet (dry) events are selected when the OLR anomalies are greater than 1 (less than −1) for wet (dry) events. The averaged areas are marked as red boxes in Fig. 4.

the ISO intensity is located along 15°N over the Philippine Sea, the South China Sea, the Bay of Bengal, and the eastern Arabian Sea, whereas the most pronounced year-to-year variation in summer mean state is located over the equatorial region (Teng and Wang 2003). In other words, the difference in sensitive location between intraseasonal and interannual variabilities over Asia–Pacific region provides a possibility that particular phases can be more favorable for interannual variability such as ENSO. For

this reason, we further examine the relationship between the annual occurrences of four major phases identified by ESOM analysis and preceding ENSO variability.

Figure 10 shows correlation coefficient between preceding wintertime SST (Figs. 10a–d) and springtime geopotential height at 850 hPa (Figs. 10e–h) and the annual number of clustered days in four major phases. The most significant correlations are seen in phases 3 and 7. Especially, phase 3 is positively (negatively) correlated to the preceding wintertime SST over the eastern Indian Ocean, Philippine Sea, and eastern Pacific (off-equatorial central Pacific) (Fig. 10b). The springtime geopotential height field at 850 hPa shows positive correlation tilted from northwest to southeast (Fig. 10f). The axis of the maximum positive correlation coincides with the negative OLR region in phase 3 in Fig. 4. Another positive correlation is found over southern Japan along 30°N. On the contrary, phase 7 shows negative correlation with preceding wintertime SST centered at the southeastern Indian Ocean (Fig. 10d). In addition, negative correlation with springtime geopotential height is located over the subtropical western Pacific along 10°N.

We further examined the changes in annual occurrence of each phase based on different phases of ENSO. We found that the annual occurrence of phase 3 is increased (decreased) by 20% (16%) and that of phase 4 is decreased (increased) by 14% (6%) during El Niño decaying (La Niña decaying) summer. The other two phases (i.e., phases 1 and 5) do not display significant changes in annual occurrence during El Niño decaying summer. It is also identified that the annual occurrences of phases 3 and 7 are positive related to the El Niño developing summer, whereas those of phases 1 and 5 are negatively related (figure not shown). In summary, El Niño–related SST warming (cooling) over the eastern Pacific and eastern Indian Ocean provides favorable condition for phase 3 (phase 7) to happen more (less) frequently after El Niño decaying. Although the asymmetry in the eastern Indian Ocean convection between phases 3 and 7 mentioned in section 4c is independent from ENSO, we further found that the two phases are related to the asymmetric large-scale forcing.

5. Summary and discussion

The boreal BSISO is a dominant mode of intraseasonal variability in the tropics during the boreal summer (May to October). The BSISO exhibits more complex features than wintertime MJO because it involves northward propagation and interactions with ISM and EASM, which makes it difficult to understand irregular spatiotemporal characteristics of BSISO. In this study, we applied the EOF-based nonlinear SOM

CC with SST (DJF)

(a) Phase1

(b) Phase3

(c) Phase5

(d) Phase7

CC with Z850 (MAM)

(e) Phase1

(f) Phase3
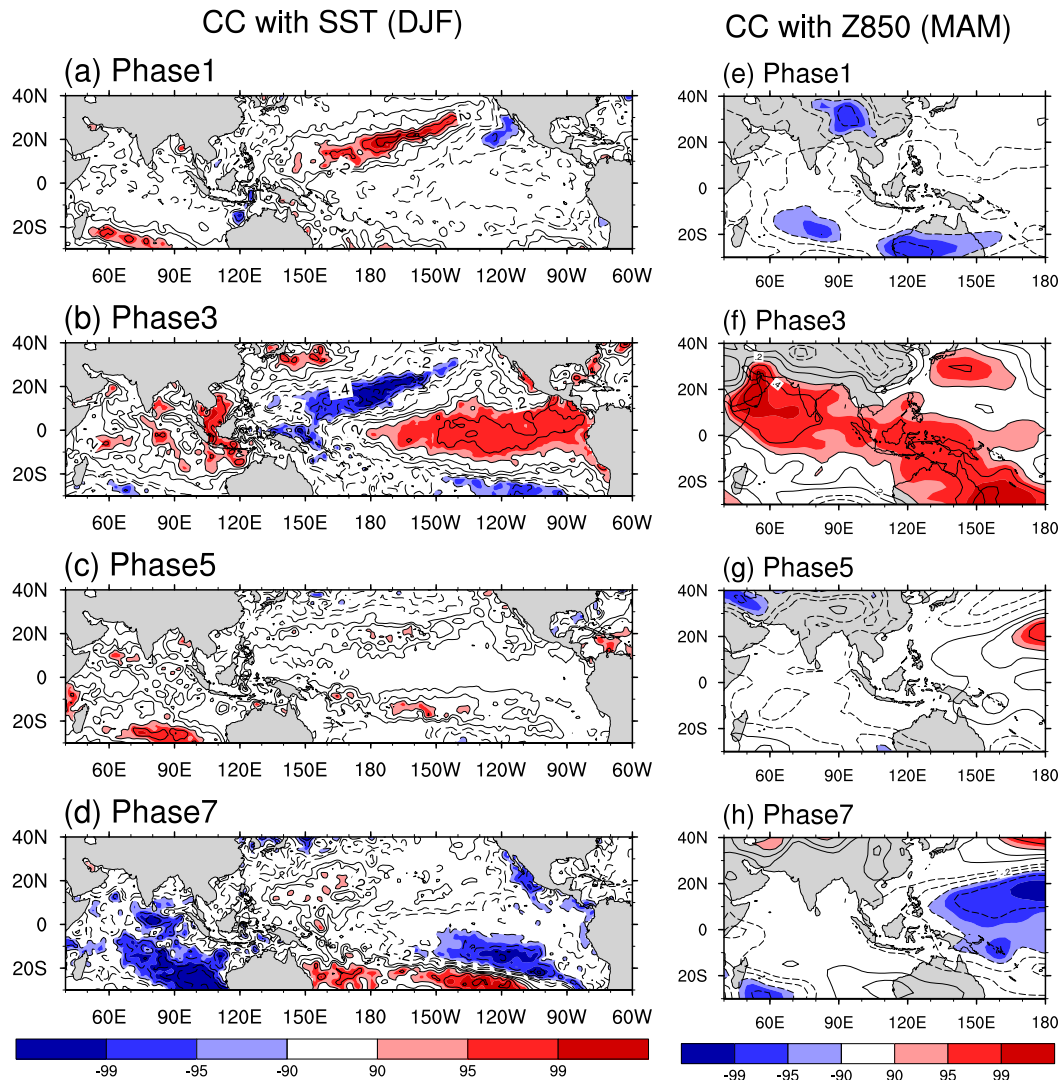
(g) Phase5

(h) Phase7

FIG. 10. The correlation coefficients of interannual variability of four major phases with (a)–(d) preceding wintertime (DJF) SST anomalies and (e)–(h) springtime (MAM) geopotential anomalies at 850 hPa. The interannual variability of the four phases are defined as the annual number of clustered days at each mode. Contour indicates the correlation coefficients with an interval of 0.1. Shading indicates statistically significant areas.

technique (ESOM) using a synthetic PC time series of OLR and U850 over ASM region. The ESOM analysis has advantages in filtering out uncertainties from high-frequency noise and being free from mathematical restrictions, such as orthogonality and linearity. More importantly, the ESOM analysis can offer additional information that the EOF analysis cannot offer, such as nonlinear preferred seasonal occurrence and phase locking, stationary and transitional characteristics, nonlinear evolution of convective activities, and asymmetric response to large-scale SST forcing. The ESOM analysis projects BSISO phases projected to the 3 × 3 lattice, with similar patterns nearby and dissimilar patterns farther apart.

Lee et al. (2013) have demonstrated the existence of a dipole between the eastern Indian Ocean and the Philippine Sea, and a northwest–southeast-tilted rain belt structure using MV-EOF analysis. We confirmed that two pairs of ESOM patterns are similar to the first two leading MV-EOF modes, and they explain alternative oscillation throughout the entire summer with an approximate 30–60-day period. The ESOM enables to detect the 30–60-day cycle of northward-propagating BSISO.

We have also demonstrated the new features of BSISO revealed by ESOM analysis in terms of four dominant phases. The horizontal patterns of individual phases are described in Fig. 4.

1) Phase 1 and phase 5 have similar horizontal structures with the first MV-EOF mode and show alternating oscillations throughout the entire summer with an approximate 30–60-day period supporting the existence of a climatological intraseasonal oscillation. On the contrary, phase 3 and phase 7 have distinct preference in occurrence during a certain time period. Phase 3 peaks in mid-June denoting the significant rainy season of the ASM, while phase 7 peaks on 1 June, denoting the local premonsoon states in the ISM and EASM. The results suggest that phase locking of the ASM is contingent on the occurrence of these northwest–southeast-tilted rain belt phases (i.e., phase 3 and phase 7).

2) The ESOM enables the depiction of different stationary and propagating characteristics of the individual phases. We found that the phases related to a dipole pattern (phase 1 and phase 5) happen more frequently and last longer than the phases with quadrupole patterns (phase 3 and phase 7), whereas MV-EOF analysis fails to describe the nonlinear occurrences.

3) There is apparent asymmetry between phase 3 and phase 7 over the eastern Indian Ocean. Composite analysis of positive and negative convective events revealed that the asymmetry is related to the slow-growing and fast-decaying convective activity, and this feature is the intrinsic property of the tropical Indian Ocean independent of ENSO events.

4) El Niño–related SST warming (cooling) over the eastern Pacific and eastern Indian Ocean provides favorable conditions for phase 3 (phase 7) to happen more (less) frequently after El Niño decaying summer. In addition, the annual occurrences of phase 3 and phase 7 are positive related to the El Niño developing summer, whereas those of phase 1 and phase 5 are negatively related.

This paper suggests that ESOM is a useful mathematical tool for extracting BSISO signals and providing new features detected by nonlinear ESOM analysis over other linear analysis. We believe that the application of nonlinear ESOM phases on intraseasonal forecast will be useful for real-time monitoring and forecast. For example, the time series of four BSISO phases can be calculated by projecting ESOM patterns on the daily OLR anomaly, which enables monitoring real-time ISO behavior. The optimal method for applying ESOM phases on intraseasonal forecast should be carefully developed and further investigated.

REFERENCES

Annamalai, H., and M. J. Slingo, 2001: Active/break cycles: Diagnosis of the intraseasonal variability of the Asian summer monsoon. *Climate Dyn.*, **18**, 85–102, doi:10.1007/s003820100161.

Borah, N., A. K. Sahai, R. Chattopadhyay, S. Joseph, S. Abhilash, and B. N. Goswami, 2013: A self-organizing map–based ensemble forecast system for extended range prediction of active/break cycles of Indian summer monsoon. *J. Geophys. Res. Atmos.*, **118**, 9022–9034, doi:10.1002/jgrd.50688.

Chattopadhyay, R., A. K. Sahai, and B. N. Goswami, 2008: Objective identification of nonlinear convectively coupled phases of monsoon intraseasonal oscillation: Implications for prediction. *J. Atmos. Sci.*, **65**, 1549–1569, doi:10.1175/2007JAS2474.1.

——, A. Vintzileos, and C. Zhang, 2013: A description of the Madden–Julian oscillation based on a self-organizing map. *J. Climate*, **26**, 1716–1732, doi:10.1175/JCLI-D-12-00123.1.

Chu, J.-E., S. N. Hameed, and K.-J. Ha, 2012: Nonlinear, intraseasonal phases of the East Asian summer monsoon: Extraction and analysis using self-organizing maps. *J. Climate*, **25**, 6975–6988, doi:10.1175/JCLI-D-11-00512.1.

Ding, Q., and B. Wang, 2009: Predicting extreme phases of the Indian summer monsoon. *J. Climate*, **22**, 346–363, doi:10.1175/2008JCLI2449.1.

Ding, Y., and L. J. C. Chan, 2005: The East Asian summer monsoon: An overview. *Meteor. Atmos. Phys.*, **89**, 117–142, doi:10.1007/s00703-005-0125-z.

Hsu, P.-C., J.-Y. Lee, and K.-J. Ha, 2016: Influence of boreal summer intraseasonal oscillation on rainfall extremes in southern China. *Int. J. Climatol.*, **36**, 1403–1412, doi:10.1002/joc.4433.

Johnson, N. C., 2013: How many ENSO flavors can we distinguish? *J. Climate*, **26**, 4816–4827, doi:10.1175/JCLI-D-12-00649.1.

Joseph, S., A. K. Sahai, R. Chattopadhyay, and B. N. Goswami, 2011: Can El Niño–Southern Oscillation (ENSO) events modulate intraseasonal oscillations of Indian summer monsoon? *J. Geophys. Res.*, **116**, D20123, doi:10.1029/2010JD015510.

Kajikawa, Y., and T. Yasunari, 2005: Interannual variability of the 10–25- and 30–60-day variation over the South China Sea during boreal summer. *Geophys. Res. Lett.*, **32**, L04710, doi:10.1029/2004GL021836.

Kanamitsu, M., and Coauthors, 2002: NCEP dynamical seasonal forecast system 2000. *Bull. Amer. Meteor. Soc.*, **83**, 1019–1037, doi:10.1175/1520-0477(2002)083<1019:NDSFS>2.3.CO;2.

Kang, I.-S., C.-H. Ho, Y.-K. Lim, and K.-M. Lau, 1999: Principal modes of climatological seasonal and intraseasonal variations of the Asian summer monsoon. *Mon. Wea. Rev.*, **127**, 322–340, doi:10.1175/1520-0493(1999)127<0322:PMOCSA>2.0.CO;2.

Kemball-Cook, S., and B. Wang, 2001: Equatorial waves and air–sea interaction in the boreal summer intraseasonal oscillation. *J. Climate*, **14**, 2923–2942, doi:10.1175/1520-0442(2001)014<2923:EWAASI>2.0.CO;2.

Kohonen, T., 1982: Self-organized formation of topologically correct feature maps. *Biol. Cybern.*, **43**, 59–69, doi:10.1007/BF00337288.

——, 1990: The self-organizing map. *Proc. IEEE*, **78**, 1464–1480, doi:10.1109/5.58325.

——, 1997: *Self-Organizing Maps*. 2nd ed. Springer Series in Information Sciences, Vol. 30, 426 pp.

Lau, K.-M., and P. H. Chan, 1986: Aspects of the 40–50 day oscillation during the northern summer as inferred from outgoing longwave radiation. *Mon. Wea. Rev.*, **114**, 1354–1367, doi:10.1175/1520-0493(1986)114<1354:AOTDOD>2.0.CO;2.

Lee, J.-Y., and Coauthors, 2010: How are seasonal prediction skills related to models' performance on mean state and annual cycle? *Climate Dyn.*, **35**, 267–283, doi:10.1007/s00382-010-0857-4.

——, B. Wang, M. C. Wheeler, X. Fu, D. E. Waliser, and I.-S. Kang, 2013: Real-time multivariate indices for the boreal summer intraseasonal oscillation over the Asian summer monsoon region. *Climate Dyn.*, **40**, 493–509, doi:10.1007/s00382-012-1544-4.

Liebmann, B., and C. A. Smith, 1996: Description of a complete (interpolated) outgoing longwave radiation dataset. *Bull. Amer. Meteor. Soc.*, **77**, 1275–1277.

LinHo, and B. Wang, 2002: The time–space structure of the Asian–Pacific summer monsoon: A fast annual cycle view. *J. Climate*, **15**, 2001–2019, doi:10.1175/1520-0442(2002)015<2001:TTSSOT>2.0.CO;2.

Liu, B., Y. Liu, G. Wu, J. Yan, J. He, and S. Ren, 2015: Asian summer monsoon onset barrier and its formation mechanism. *Climate Dyn.*, **45**, 711–726, doi:10.1007/s00382-014-2296-0.

Liu, F., and B. Wang, 2014: A mechanism for explaining the maximum intraseasonal oscillation center over the western North Pacific. *J. Climate*, **27**, 958–968, doi:10.1175/JCLI-D-12-00797.1.

Liu, Y., J. C. L. Chan, J. Mao, and G. Wu, 2002: The role of Bay of Bengal convection in the onset of the 1998 South China Sea summer monsoon. *Mon. Wea. Rev.*, **130**, 2731–2744, doi:10.1175/1520-0493(2002)130<2731:TROBOB>2.0.CO;2.

——, R. H. Weisberg, and C. N. K. Mooers, 2006: Performance evaluation of the self-organizing map for feature extraction. *J. Geophys. Res.*, **111**, C05018, doi:10.1029/2005JC003117.

Madden, R. A., and P. R. Julian, 1972: Description of global-scale circulation cells in the tropics with a 40–50 day period. *J. Atmos. Sci.*, **29**, 1109–1123, doi:10.1175/1520-0469(1972)029<1109:DOGSCC>2.0.CO;2.

Oettli, P., T. Tozuka, T. Izumo, F. A. Engelbrecht, and T. Yamagata, 2014: The self-organizing map, a new approach to apprehend the Madden–Julian oscillation influence on the intraseasonal variability of rainfall in the southern African region. *Climate Dyn.*, **43**, 1557–1573, doi:10.1007/s00382-013-1985-4.

Oh, H., and K.-J. Ha, 2015: Thermodynamic characteristics and responses to ENSO of dominant intraseasonal modes in the East Asian summer monsoon. *Climate Dyn.*, **44**, 1751–1766, doi:10.1007/s00382-014-2268-4.

Sahai, A. K., R. Chattopadhyay, S. Joseph, S. Abhilash, N. Borah, and B. N. Goswami, 2014: A new method to compute the principal components from self-organizing maps: An application to monsoon intraseasonal oscillations. *Int. J. Climatol.*, **34**, 2925–2939.

Teng, H., and B. Wang, 2003: Interannual variations of the boreal summer intraseasonal oscillation in the Asian–Pacific region. *J. Climate*, **16**, 3572–3584, doi:10.1175/1520-0442(2003)016<3572:IVOTBS>2.0.CO;2.

Wang, B., and X. Xie, 1997: A model for the boreal summer intraseasonal oscillation. *J. Atmos. Sci.*, **54**, 72–86, doi:10.1175/1520-0469(1997)054<0072:AMFTBS>2.0.CO;2.

——, and X. Xu, 1997: Northern Hemisphere summer monsoon singularities and climatological intraseasonal oscillation. *J. Climate*, **10**, 1071–1085, doi:10.1175/1520-0442(1997)010<1071:NHSMSA>2.0.CO;2.

——, R. Wu, and K.-M. Lau, 2001: Interannual variability of the Asian summer monsoon: Contrasts between the Indian and the western North Pacific–East Asian monsoons. *J. Climate*, **14**, 4073–4090, doi:10.1175/1520-0442(2001)014<4073:IVOTAS>2.0.CO;2.

——, P. J. Webster, and H. Teng, 2005: Antecedents and self-induction of active-break south Asian monsoon unraveled by satellites. *Geophys. Res. Lett.*, **32**, L17708, doi:10.1029/2005GL023769.

——, and Coauthors, 2009: Advance and prospectus of seasonal prediction: Assessment of the APCC/CliPAS 14-model ensemble retrospective seasonal prediction (1980–2004). *Climate Dyn.*, **33**, 93–117, doi:10.1007/s00382-008-0460-0.

Wheeler, M. C., and H. H. Hendon, 2004: An all-season real-time multivariate MJO Index: Development of an index for monitoring and prediction. *Mon. Wea. Rev.*, **132**, 1917–1932, doi:10.1175/1520-0493(2004)132<1917:AARMMI>2.0.CO;2.

Wu, G., and Y. Zhang, 1998: Tibetan Plateau forcing and the timing of the monsoon onset over South Asia and the South China Sea. *Mon. Wea. Rev.*, **126**, 913–927, doi:10.1175/1520-0493(1998)126<0913:TPFATT>2.0.CO;2.

Yasunari, T., 1979: Cloudiness fluctuations associated with the Northern Hemisphere summer monsoon. *J. Meteor. Soc. Japan*, **57**, 227–242.

——, 1980: A quasi-stationary appearance of 30 to 40 day period in the cloudiness fluctuations during the summer monsoon over India. *J. Meteor. Soc. Japan*, **58**, 225–229.

Yun, K.-S., B. Ren, K.-J. Ha, J. C. L. Chan, and J.-G. Jhun, 2009: The 30–60-day oscillation in the East Asian summer monsoon and its time-dependent association with the ENSO. *Tellus*, **61A**, 565–578, doi:10.1111/j.1600-0870.2009.00410.x.

——, K.-H. Seo, and K.-J. Ha, 2010: Interdecadal change in the relationship between ENSO and the intraseasonal oscillation in East Asia. *J. Climate*, **23**, 3599–3612, doi:10.1175/2010JCLI3431.1.

Zhu, B., and B. Wang, 1993: The 30–60-day convection seesaw between the tropical Indian and western Pacific Oceans. *J. Atmos. Sci.*, **50**, 184–199, doi:10.1175/1520-0469(1993)050<0184:TDCSBT>2.0.CO;2.